ACS Photonics

pubs.acs.org/journal/apchd5 Article

Nonreciprocal Light Propagation in a Cascaded All-Silicon Microring Modulator

Awanish Pandey,* Sarvagya Dwivedi, Tang Zhenzhou, Shilong Pan, and Dries Van Thourhout

Cite This: https://doi.org/10.1021/acsphotonics.1c00040 Read Online

ACCESS | Metrics & More | Article Recommendations

ABSTRACT: Optical isolators and circulators are critical building blocks for large-scale photonic integrated circuits. Among the several methods proposed to realize such nonreciprocal devices, including heterogeneous integration with garnet-based materials or using nonlinearities, dynamic modulation of the waveguide properties is a potentially practical and easily accessible method. However, most proposals relying on this method rely on modulators with a very large footprint, limiting their practical applicability. This paper overcomes this issue by presenting a method to achieve nonreciprocal optical transmission taking advantage of compact ring modulators. We use a cascaded system of microring modulators with a footprint as small as 15 μm × 220 μm and propose that, by tuning the relative time delay between the RF driving signals and the optical delay between the modulators, nonreciprocal transmission can be achieved. We present a detailed theoretical analysis of our design and investigate the origin of the asymmetric transmission. The modulators were designed and fabricated on IMEC's Silicon-on-Insulator platform iSiPP50G. We achieve a 16 dB difference between forward and backward optical signals at a driving voltage (V_{pp}) of 8 V at 6 GHz. Moreover, we analyze the impact of fabrication imperfections on the device performance. Our work leads to a significant reduction in device footprint compared to formerly explored solutions using dynamic modulation and is well suited for monolithic integration with photonic integrated circuits.

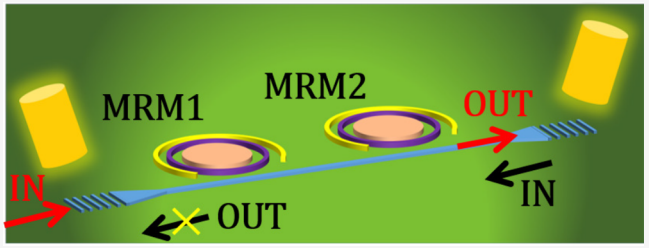

KEYWORDS: *silicon photonics, microphotonic device, microring resonators, electro-optic modulation, nonreciprocity*

INTRODUCTION

The growing maturity of photonic integrated circuits (PICs) has facilitated the realization of lasers, detectors, modulators, and sophisticated passive circuits, catering to the ever-growing demand for bandwidth and speed in optical communication networks.[1] Optical nonreciprocal transmission is a critical feature for PICs that restricts the light to travel only in the forward direction while blocking it in the backward direction. It enables components like optical isolators, circulators, and diodes and assists in all-optical signal processing.[2−4] In particular, nonreciprocity is critical for complex PICs incorporating lasers and amplifiers as it blocks back-reflections and alleviates multipath interference, thereby providing stable operation.[5] Three different methods have been explored to realize nonreciprocity for silicon-based photonic devices.

In the first method, a magneto-optic garnet material is deposited on the waveguides, and the device is immersed in a magnetic field. When well-designed, this leads to a direction-dependent phase shift for light traveling through the waveguide.[6−11] Integrating such waveguides in a Mach−Zehnder interferometer or ring resonator offers nonreciprocal transmission at a telecommunication wavelength. However, the integration of garnets with a silicon waveguide is far from straightforward. Moreover, as a magneto-optic garnet deposited on top of the waveguide typically operates in the TM-like mode, there is a need for polarization manipulators before and after the nonreciprocal phase section, further adding to the design and fabrication complexity.[12] The second method utilizes nonlinear effects like the Kerr nonlinearity.[3,13−16] In doing so, the bandwidth of operation is limited due to the stringent phase-matching conditions. Besides, it is a power-hungry scheme where nonreciprocity is strongly dependent on the pump strength. Though it is possible to lower the pump-power requirement substantially using ultra-high-quality-factor resonators,[17] the optical power required to achieve modest nonreciprocal transmission is still high. Hence, an effective one-way transmission can only be achieved with a large optical input power,[5] not compatible with practical application scenarios.

Received: January 7, 2021

https://doi.org/10.1021/acsphotonics.1c00040
ACS Photonics XXXX, XXX, XXX−XXX

The final approach exploits the spatiotemporal effective index modulation (EIM) of silicon waveguides using microwave or acoustic signals.[18−21] The modulated optical carrier is coupled either to different modes through intermode transitions as proposed in ref 22 or to the sideband frequencies as explained in ref 23. This process is dependent on the direction of the propagating optical signal, which leads to nonreciprocal transmission.

It is a simple method to achieve isolation as it does not require the deposition of extra materials or a strong pump signal and therefore forms a potential candidate for realizing a practical on-chip isolator. This scheme's disadvantage is that it requires large RF power to achieve the necessary modulation and requires a relatively large footprint.[24]

Optical isolation using EIM in silicon waveguides has been demonstrated using tandem phase modulators, interferometers, and traveling-wave modulators.[24−26] Tandem phase modulators redistribute the power in the optical carrier to the sidebands, in a way which is dependent on the direction of propagation, and allow for higher-order designs to achieve a high isolation ratio.[23,27] Interferometers are a very elegant way to achieve isolation and operate by transferring the carrier's optical energy to the different modes supported by the interferometer. In traveling-wave modulators, parallel Mach−Zehnder modulators are used where the traveling electrical waves are responsible for the direction-dependent transmission. However, all of these techniques require a large footprint. This large footprint is needed to achieve the required phase modulation as, in typical electro-optical modulators, the change in the effective index is usually in the order of 10^{-5} to 10^{-4}. For example, the length of the phase modulators used in refs 24 and 25 was 800 μm and 3.9 mm, respectively. Thus, for on-chip isolators, exploring more compact solutions is highly desirable.

In this work, we take advantage of compact microring modulators (MRMs) to significantly reduce the device footprint and obtain nonreciprocal transmission in cascaded ring modulators. The resonant nature of MRMs allows for a considerable amount of enhancement in modulation strength and equips the system with enhanced degrees of freedom to engineer their response by either coupling to different resonators or coupling to additional waveguides. Given their versatility, MRMs have already been used for several applications like wavelength division multiplexing for optical interconnection, radio over fiber, and frequency comb generation.[28−30] There has also been a theoretical proposal to utilize MRMs for lossless frequency conversion where the optical carrier can be completely converted into sideband frequencies.[31] More recently MRMs were also proposed as a route toward realizing an optical isolator.[32] However, a rigorous theoretical analysis, as well as an experimental demonstration, has not been shown yet.

The proposed design is shown in Figure 1a. It consists of two MRMs sharing the same bus waveguide, separated by a distance L. This is equivalent with a time delay $\tau_0 = L/v_g$ with v_g the optical group velocity in the waveguide. Both MRMs are identical. They have a radius of 5 μm and a gap of 180 nm between the ring and bus waveguide. The waveguides forming the MRM are 500 nm wide and etched 150 nm deep into a 220 nm thick silicon layer. The optical delay length L is 200 μm, which corresponds with a time delay of 1.6 ps. The waveguide connecting the MRMs is a fully etched strip waveguide. The devices were fabricated on IMEC's iSIPP50G silicon photonics platform.[33] Figure 1b shows a microscope image of the fabricated device. The footprint of the device, without the contacts, is 15 μm × 200 μm. A more detailed profile of the device is shown in Figure 1c depicting the cross-section of the waveguide, the doping profile forming the pn-junction needed to achieve EIM, the Tungsten contact plugs, the Cu interconnects, and the AlCu bondpads for applying the electrical signal.

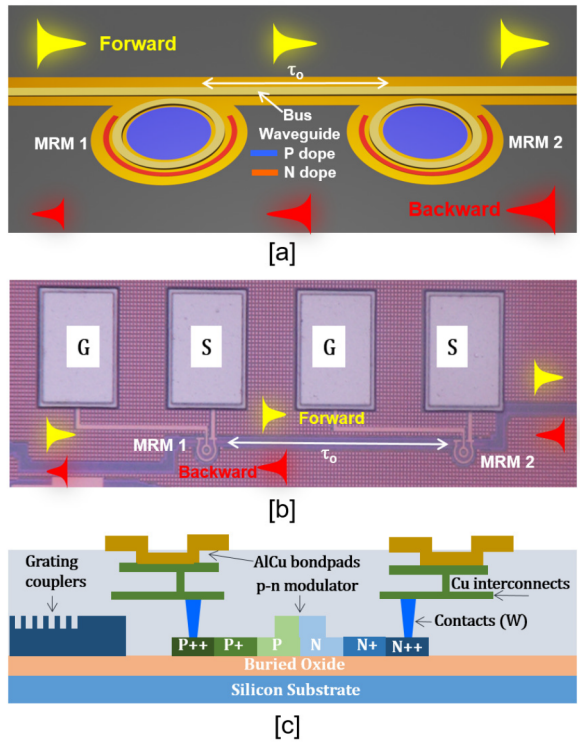

Figure 1. (a) Schematic of the proposed cascaded ring modulator. (b) Microscope image of the fabricated device. (c) Various connections and doping profile of the device. Both ring modulators are driven using a single GSGS probe.

We first present a theoretical framework describing the operation of our device by extending the analysis proposed in refs 34 and 35 and investigate the origin of nonreciprocal transmission in our device. We also discuss the conditions for the optimum performance of our device. We then proceed to describe the experimental setup and subsequently discuss the results obtained.

Theoretical Framework and Simulations. The schematic of a single MRM is shown in Figure 2. A p-n-doped ring modulator is evanescently coupled to a bus waveguide. The input to the modulator is a continuous wave optical carrier that is modulated by applying an RF signal in the MRM. The

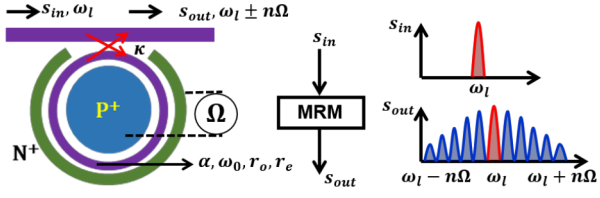

Figure 2. Schematic of a single MRM. The optical input is modulated by the MRM, driven by an RF input, and the output is the optical carrier flanked by sidebands separated by $n\Omega$.

https://doi.org/10.1021/acsphotonics.1c00040
ACS Photonics XXXX, XXX, XXX−XXX

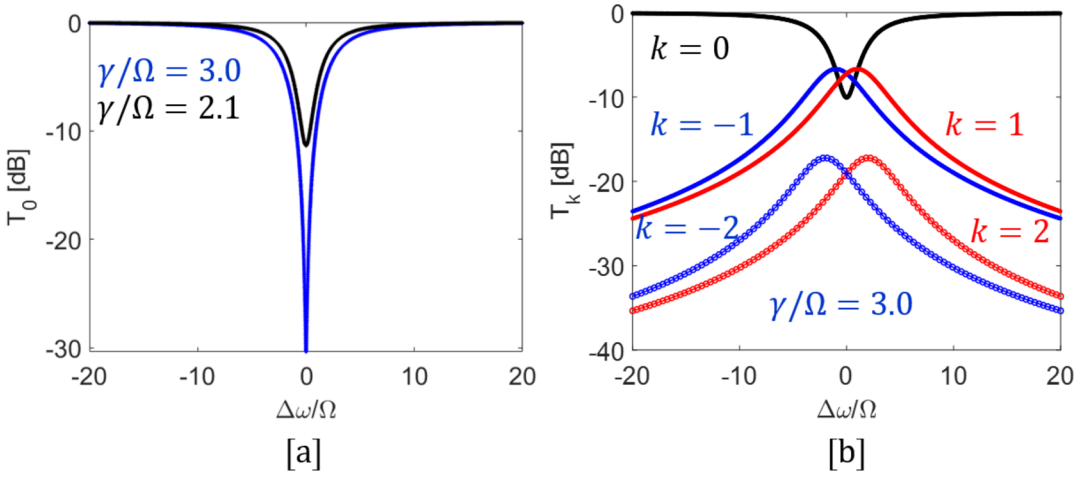

Figure 3. (a) Transmission of an unmodulated cavity ($\frac{\delta\omega}{\Omega} = 0$) with different γ' values. (b) Variation of sideband components as well as the optical carrier for a modulated microring with $\frac{\delta\omega}{\Omega} = 2.1$.

coupled mode equation for the optical wave amplitude $\alpha(t)$ in the MRM can be written as[31,34,36]

$$\frac{d\alpha}{dt} = (i\omega_0 + i\delta\omega(t) - \gamma')\alpha - i\sqrt{2\gamma}s_+ \tag{1}$$

and the wave amplitude at the output is obtained as

$$s_- = s_+ - i\sqrt{2\gamma}\alpha(t) \tag{2}$$

where s_+ is the input optical signal, s_- the output optical signal from the MRM, and ω_0 the natural resonance of the microring without applied bias; $\delta\omega(t)$ describes how this frequency is changed by the applied RF-wave, and α is the amplitude of the resonant mode with $|\alpha^2|$ representing the optical energy in the cavity. The decay rate of α due to the bus-to-ring coupling is given by $\gamma = \frac{\kappa^2 v_g}{2L}$, with κ the coupling coefficient between the ring and the waveguide. The total decay rate is then given by $\gamma' = \gamma + \gamma_l$ where γ_l is the decay rate due to losses inside the ring. Applying an external RF voltage $V(t) = V_{rf}\cos(\Omega t)$ results in a modulation $\delta\omega(t) = \delta\omega\cos(\Omega t)$ of the central frequency ω_0. We have $\delta\omega_{m1} = \frac{\delta\omega_0}{\delta V_{RF^1}}V_{RF}$ where $\frac{\delta\omega_0}{\delta V_{RF}}$ is the change in resonance frequency of the ring per volt of applied RF signal. For an input source $s_+ = Ae^{i\omega_l t}$, the solution for the first-order differential eq 1 takes the following form:

$$\frac{s_-}{s_+} = 1 - \frac{\gamma}{\Omega}\sum_{m=-\infty}^{\infty}\sum_{n=-\infty}^{\infty}\frac{(-1)^n J_n\left(\frac{\delta\omega}{\Omega}\right)J_m\left(\frac{\delta\omega}{\Omega}\right)e^{-i(n+m)\Omega t}}{\frac{\gamma'}{2\Omega} + i\frac{\Delta\omega}{\Omega} + in} \tag{3}$$

where $\Delta\omega = \omega_l - \omega_0$ is the source frequency detuning from the ring resonance ($\Delta\omega = 0$ at the resonance), and $J_n(z)$ is the nth order Bessel function of the first kind with the argument z.

Equation 3 is consistent with the solution obtained in refs 34 and 35. It represents an output signal consisting of a carrier and a series of sidebands separated by $(n + m)\Omega$ from the carrier frequency ω_l. The total transmission in a particular sideband k (T_k) or in the carrier (T_0) can be obtained by collecting all terms with that particular frequency. For example, the first-order sideband transmission is obtained by collecting all terms oscillating at $\omega_l + \Omega$.

Figure 3 shows the response of a single resonator based on the analysis above. In Figure 3a, the passive response of the MRM is shown for two different values of $\frac{\gamma'}{\Omega}$. For $\frac{\gamma'}{\Omega} = 2.1$ (γ = 9 GHz, γ_l = 3.6 GHz, Ω = 6 GHz), a resonance dip is observed at $\frac{\Delta\omega}{\Omega} = 0$. The resonance becomes wider when $\frac{\gamma'}{\Omega}$ is increased to 3.0 by increasing the value for γ_l as the quality factor of the resonance decreases with increasing loss. Figure 3b shows the transmission of the optical carrier and the generated sidebands vs the detuning $\Delta\omega/\Omega$, for $\delta\omega/\Omega = 2.1$ and $\gamma'/\Omega = 3.0$. It can be seen that the carrier goes through a minimum at $\Delta\omega/\Omega = 0$ while the sidebands T_m values peak at $\Delta\omega/\Omega = m$ with their amplitude determined by eq 3.

For cascaded MRMs, the transfer function of each modulator in the forward and backward directions is obtained in the following manner:

$$T^{1,\text{forw.}}(\Delta\omega, t) = 1 - \frac{\gamma}{\Omega}\sum_{m=-\infty}^{\infty}\sum_{n=-\infty}^{\infty}\frac{(-1)^n J_n\left(\frac{\delta\omega}{\Omega}\right)J_m\left(\frac{\delta\omega}{\Omega}\right)e^{-i(n+m)\Omega(t-\tau_0)}}{\frac{\gamma'}{2\Omega} + i\frac{\Delta\omega}{\Omega} + in} \tag{4}$$

$$T^{2,\text{forw.}}_{n,m}(\Delta\omega + (n+m)\Omega, t) = 1 - \frac{\gamma}{\Omega}\sum_{m'=-\infty}^{\infty}\sum_{n'=-\infty}^{\infty}\frac{(-1)^{n'} J_{n'}\left(\frac{\delta\omega}{\Omega}\right)J_{m'}\left(\frac{\delta\omega}{\Omega}\right)e^{-i(n'+m')\Omega(t+\tau_{rf})}}{\frac{\gamma'}{2\Omega} + i\frac{\Delta\omega + (n+m)\Omega}{\Omega} + in'} \tag{5}$$

In the backward direction, the equations are

$$T^{2,\text{back.}}(\Delta\omega, t) = 1 - \frac{\gamma}{\Omega}\sum_{m=-\infty}^{\infty}\sum_{n=-\infty}^{\infty}\frac{(-1)^n J_n\left(\frac{\delta\omega}{\Omega}\right)J_m\left(\frac{\delta\omega}{\Omega}\right)e^{-i(n+m)\Omega(t-\tau_0+\tau_{rf})}}{\frac{\gamma'}{2\Omega} + i\frac{\Delta\omega}{\Omega} + in} \tag{6}$$

$$T^{1,\text{back.}}_{n,m}(\Delta\omega + (n+m)\Omega, t) = 1 - \frac{\gamma}{\Omega}\sum_{m'=-\infty}^{\infty}\sum_{n'=-\infty}^{\infty}\frac{(-1)^{n'} J_{n'}\left(\frac{\delta\omega}{\Omega}\right)J_{m'}\left(\frac{\delta\omega}{\Omega}\right)e^{-i(n'+m')\Omega t}}{\frac{\gamma'}{2\Omega} + i\frac{\Delta\omega + (n+m)\Omega}{\Omega} + in'} \tag{7}$$

To obtain the final transmission, T_f, the sidebands as well as the carrier components from the first modulator are provided to the second modulator. Each of these components is then modulated by the second modulator, which results in a new series of sidebands. Hence, in eqs 5 and 7, the term $\frac{\Delta\omega}{\Omega}$ in the

https://doi.org/10.1021/acsphotonics.1c00040
ACS Photonics XXXX, XXX, XXX−XXX

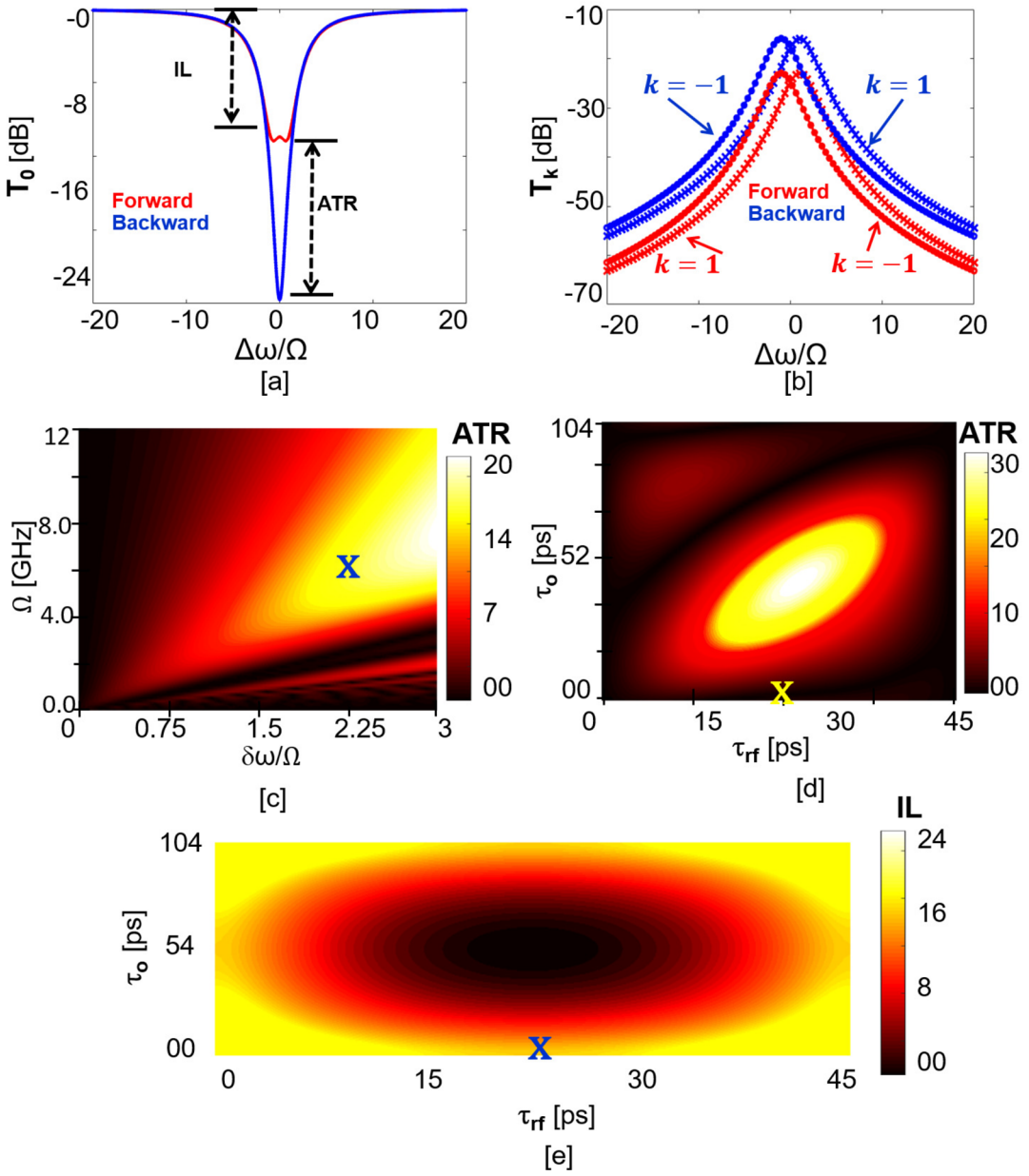

Figure 4. Transmission of cascaded MRMs: (a) forward and backward direction for the optical carrier showing the asymmetric transmission ratio (ATR) and insertion loss (IL) in the forward direction and (b) forward and backward transmission for the first-order sidebands for τ_0 = 1.6 ps and τ_{rf} = 22.5 ps. (c) ATR as a function of driving frequency (Ω) and the MRM resonance modulation frequency $\delta\omega$ for τ_0 = 1.6 ps and τ_{rf} = 22.5 ps. (d) Variation of ATR when the RF and optical delay are varied at Ω = 6 GHz, and (e) variation of insertion loss with the optical and RF delay at Ω = 6 GHz.

denominator has been modified toward $\frac{\Delta\omega + (n+m)\Omega}{\Omega}$ to take into account the excitation of the second MRM by the different sidebands generated from the first modulator. Finally, the components oscillating at particular frequencies from the second modulator are collected and analyzed for their nonreciprocal behavior. Figure 4 shows the response of the cascaded MRM device in the forward and backward direction, as a function of different modulation parameters. To quantify the nonreciprocal transmission, we define the asymmetric transmission ratio (ATR) as the difference between the transmission in the forward and backward direction. It is calculated as $10 \log_{10} T_f^{forw.} - 10 \log_{10} T_f^{back.}$.

Figure 4a shows the transmission of the optical carrier in the forward and backward direction for τ_0 = 1.6 ps, τ_{rf} = 22.5 ps, $\delta\omega/\Omega$ = 2.1, γ'/Ω = 3.0, and Ω = 6 GHz. The parameters chosen are similar to those used in the measurements reported later in this Article. The insertion loss is defined as the loss suffered by the optical carrier in the forward direction. Figure 4b shows the transmission of the sidebands for the same parameters in both directions. While for the optical carrier the insertion loss is considerably lower in the forward direction compared to the backward direction, this is the opposite for the sidebands. This already suggests that there is a direction-dependent power transfer between the optical carrier and the sidebands, which results in a nonreciprocal transmission. We will elaborate on this further below.

Figure 4c shows the variation of ATR as a function of $\frac{\delta\omega}{\Omega}$ and driving frequency Ω. We observe that, for a given $\frac{\delta\omega}{\Omega}$, there

https://doi.org/10.1021/acsphotonics.1c00040
ACS Photonics XXXX, XXX, XXX−XXX

exists a narrow band of the driving frequency, Ω, that results in the maximum ATR. For our fabricated device, $\delta\omega$ = 13.5 GHz, and the operation point is cross-marked in Figure 4d. Since the optical spectrum analyzer we later use in our experiment is resolution limited to 3.75 GHz, we select 6 GHz as our driving frequency to neatly resolve the carrier and sidebands in the analyzer. Figure 4d shows how the ATR varies as a function of τ_{rf} and τ_0 for $\frac{\delta\omega}{\Omega} = 2.1$. As observed, a maximum ATR of 30 dB is obtained when τ_0 = 51 ps, and τ_{rf} = 22.5 ps. However, a large τ_0 requires a long delay line connecting both ring resonators and hence a larger footprint. Therefore, we chose a smaller time delay of 1.6 ps, cross-marked in Figure 4c, to realize a compact nonreciprocal device while retaining a sufficiently large transmission difference between the forward and backward transmission, relevant for practical applications. In future implementations, a longer optical delay can be explored, either using a standard waveguide curled up in a spiral shape to reduce the overall size or using alternative approaches to increase the time delay within a given footprint like slow-light or multipass photonic structures.[39,40] Furthermore, our analysis also showed that the curve is periodic in nature, with a period of τ_{rf} = 45 ps, τ_0 = 104 ps, so the same ATR can be achieved over a wide range of parameters. It should be noted that if either τ_{rf} or τ_0 is zero, then nonreciprocal transmission will not exist. This is also directly obvious from eqs 4−7. A nonzero τ_{rf} ensures that both modulators are driven at different voltages as a function of time, and hence, the temporal effective index profile of each microring is different. Together with a nonzero value for τ_0, this then ensures a nonreciprocal transmission. The variation of insertion loss (IL) as a function of optical and RF delay is shown in Figure 4e. The nonreciprocal transmission is almost lossless for τ_0 = 51 ps (equivalent waveguide length in the order of 5 mm) and τ_{rf} = 22.5 ps, which is also the point for maximum ATR. It represents the parameter combination for which the most efficient transfer of optical power between the carrier and the sideband takes place.

The operating principle of the device is further elucidated in Figure 5. The two modulators are separated by an optical delay and driven by the same RF source with a relative time delay between them. In the forward direction, the optical carrier, aligned with the resonance frequency of the resonator ($\Delta\omega$ = 0), is first modulated by MRM1 resulting in the generation of sidebands at both sides of the carrier. The carrier and sidebands now act as the input to MRM2 where they are again modulated. For an appropriate choice of the optical and RF delays and the properties of the ring, the optical power in the sideband is coupled back to the carrier. As a result, the strength of the sidebands reduces while the power in the optical carrier increases. If we operate at τ_0 = 51 ps and τ_{rf} = 22.5 ps, then the power in the sidebands at the output of MRM2 will be minimized while being maximized in the carrier. In the backward direction, the distribution of power happens from the carrier to the sidebands. The optical carrier is now injected in MRM2, which produces a spectrum with the carrier and sidebands. This spectrum acts as the input to MRM1, which transfers the power from the carrier further to the sidebands. In this way, nonreciprocal transmission is attained in the cascaded ring modulator systems.

The redistribution of optical power between the carrier and the sidebands is further validated by numerically simulating the electrical field distribution associated with the carrier and various sidebands separately, in both propagating directions.

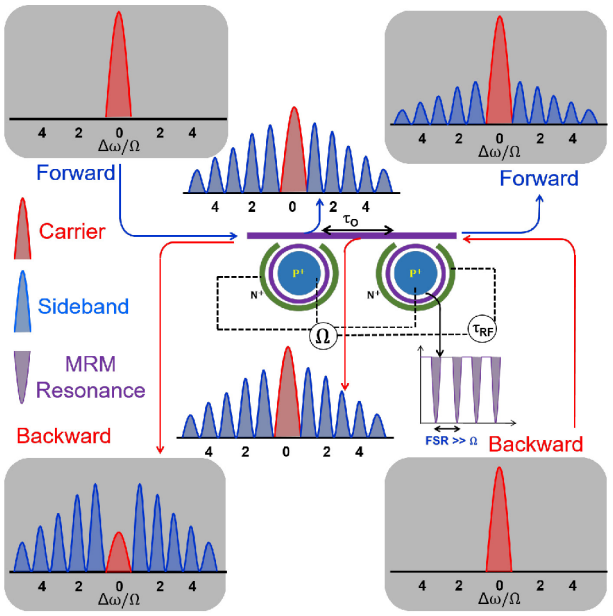

Figure 5. Operating principle of the nonreciprocal transmission in a cascaded MRM.

We use the finite difference frequency domain (FDFD) method proposed in refs 37 and 38 to study the dynamics of the active devices and adapted the code for the cascaded ring modulator configuration. The transverse E-field distribution is shown in Figure 6. It is clearly observed that, in the forward direction, the amplitude of the E-field associated with the carrier is enhanced by MRM2 while the sideband, shown for n = −1, is becoming depleted. In the backward direction, the opposite happens, and the E-field associated with the sideband is enhanced while the carrier becomes depleted.

Experimental Setup. The experimental setup used is shown in Figure 7. A tunable laser source (TLS) with 7 dBm output power serves as the device input. Polarization controllers (PCs) at the input as well as the output allow the alignment of the polarization of the forward and the backward propagating wave, respectively. The modulators are driven by a single-tone RF source that is equally divided using a 3 dB splitter, and a tunable time delay (TDL) unit is placed in one of the arms. Since the delay of the TDL is dependent on the RF frequency, it is tuned every time Ω is changed to attain the maximum ATR. The RF amplifier has a gain of 22 dB and provides a constant output V_{pp} of 8 V until 13 GHz, which then reduces to 4 V at 20 GHz. The free spectral range of the MRMs is 2500 GHz. This eliminates the possibility of transitions between modes associated with different FSRs of the resonator, leading to single-mode operation over the driving frequency range of this work.[19] We measured the back reflections from the device by putting an optical circulator between points 1 and 2. By aligning the TLS wavelength at the resonance of one of the MRMs, the back-reflected power was found to be 35 dB lower than the output power from the MRM measured at point 3.

The forward (backward) propagation is accomplished by connecting 1 → 2 and 3 → 4 (1 → 3 and 2 → 4) in Figure 7. In the forward direction, PC_1 is optimized for the maximum optical output power from the chip. Similarly, when 1 → 3 and 2 → 4 are connected, PC_2 is optimized.

https://doi.org/10.1021/acsphotonics.1c00040
ACS Photonics XXXX, XXX, XXX−XXX

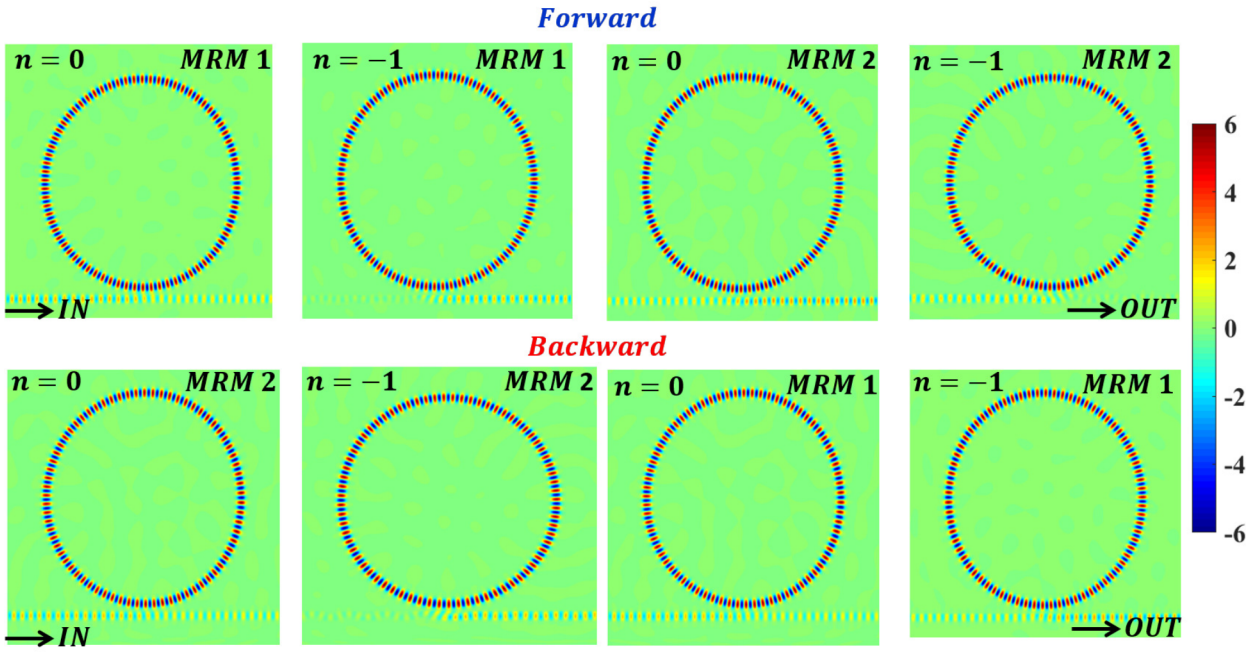

Figure 6. E-field profile of the optical carrier and $n = -1$ sideband. In the forward direction, MRM2 redistributes the sideband energy to the carrier whereas energy is transferred to the sideband from the carrier in the backward direction.

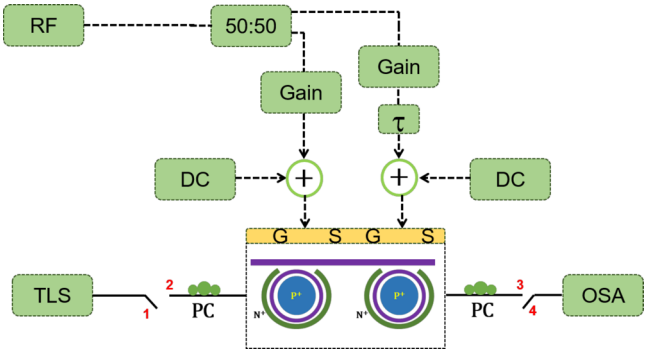

Figure 7. Experimental setup. TLS, tunable laser source; PC, polarization controller; OSA, optical spectrum analyzer; DC, DC bias; Gain, RF gain; τ_{rf}, RF delay. The connection 1 → 2 and 3 → 4 is for the forward direction, and the connection 1 → 3 and 2 → 4 is for the backward direction.

Figure 8a shows the measured response of the cascaded modulator and the associated fit, without applying a modulation voltage. Light is coupled in and out of the silicon chip using grating couplers with 11 dB/coupler loss. Due to fabrication imperfections, the resonance wavelength from both cavities will differ by a value of $\lambda_2 - \lambda_1$ as shown in Figure 8a. The variation in $\lambda_2 - \lambda_1$ vs applied bias is numerically calculated by a sequential simulation involving the Lumerical modules CHARGE, MODE, and FDTD. The dopant profile in the silicon waveguide with an applied voltage is determined from CHARGE, and using this doping profile, the variation in the effective index is calculated in MODE. This index is then supplied to FDTD to calculate the resonance shift with the applied bias. The measured and simulated variation of $\lambda_2 - \lambda_1$ with the applied DC bias on the individual modulators is shown in Figure 8b. Since, with the increasing reverse bias, the resonance undergoes a red-shift, $\lambda_2 - \lambda_1$ either decreases or increases depending upon which MRM the DC bias is applied to. We measure a wavelength shift of 13.5 GHz for 8 V of applied reverse bias for each MRM. It is worth mentioning that if a different bias is applied on the cavities, $\lambda_2 - \lambda_1$ might increase to a value where there is no overlap between the two resonances, and hence any carrier signal will be modulated by at most a single cavity, leading to the absence of nonreciprocal transmission. Further on, we will denote the wavelength of operation as λ_w.

RESULTS

In Figure 9, we characterize the nonreciprocal transmission as a function of different parameters. Figure 9a shows the backward and forward transmission at Ω = 6 GHz, 8.0 V_{pp} (22 dBm, assuming a 50 Ohm impedance), $\lambda_2 - \lambda_1$ = 8.4 GHz, and $\delta\omega$ = 13.5 GHz. The curve is normalized with the transmission of a straight waveguide to remove the loss from grating couplers and PCs. As already discussed, the strongest component in the forward direction is the optical carrier while, in the backward direction, the carrier is completely suppressed, and the optical power in the sidebands increases. We achieve an ATR of 16 dB, in-line with our simulations (Figure 4d). Without any modulation, a difference of 0.4 dB was observed between the forward and backward wave, which is attributed to the disturbance in the setup while reconnecting the optical fibers for the measurements. Figure 9b,c depicts the asymmetric transmission for Ω = 13 and 20 GHz, respectively. The increase in the driving frequency reduces the value of $\delta\omega/\Omega$, and hence, a complete suppression of the optical carrier is not attainable in such cases. Although the ATR is still 8 dB at the 13 GHz frequency, it is obvious that the carrier is less strongly suppressed in the backward direction compared to the 6 GHz case. For the 20 GHz driving frequency, we do not see any variation in the optical carrier as V_{pp} is limited to 4 V (16 dBm) at this frequency, which leads to a very small value of $\delta\omega/\Omega$. In the forward direction after removing the additional losses from the grating couplers, the insertion loss is 18, 19, and 22 dB for 6, 13, and 20 GHz driving frequencies, respectively.

https://doi.org/10.1021/acsphotonics.1c00040
ACS Photonics XXXX, XXX, XXX−XXX

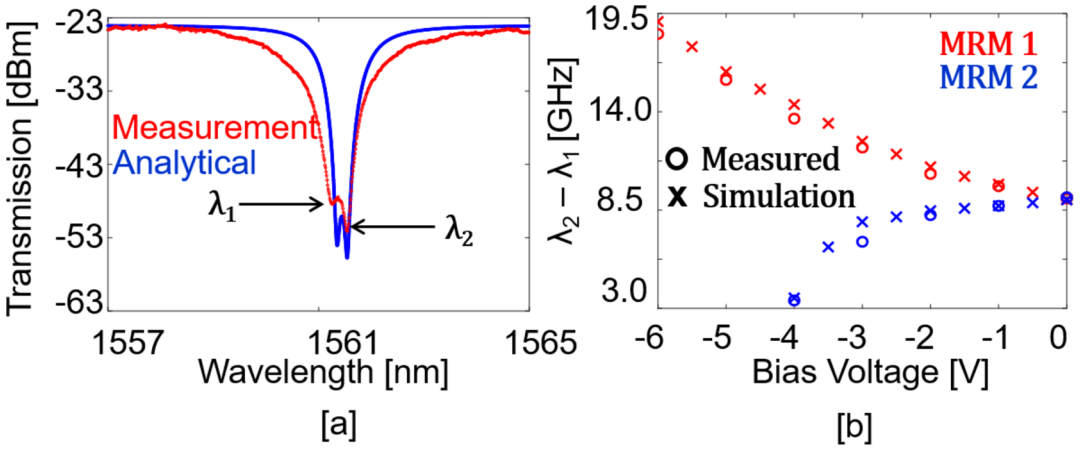

Figure 8. (a) Measured and simulated transmission spectra of the cascaded modulator. The quality factor of the individual resonators was measured to be around 17 000. (b) Variation of $\lambda_2 - \lambda_1$ when the bias of an individual modulator is varied, while keeping the other modulator at zero bias.

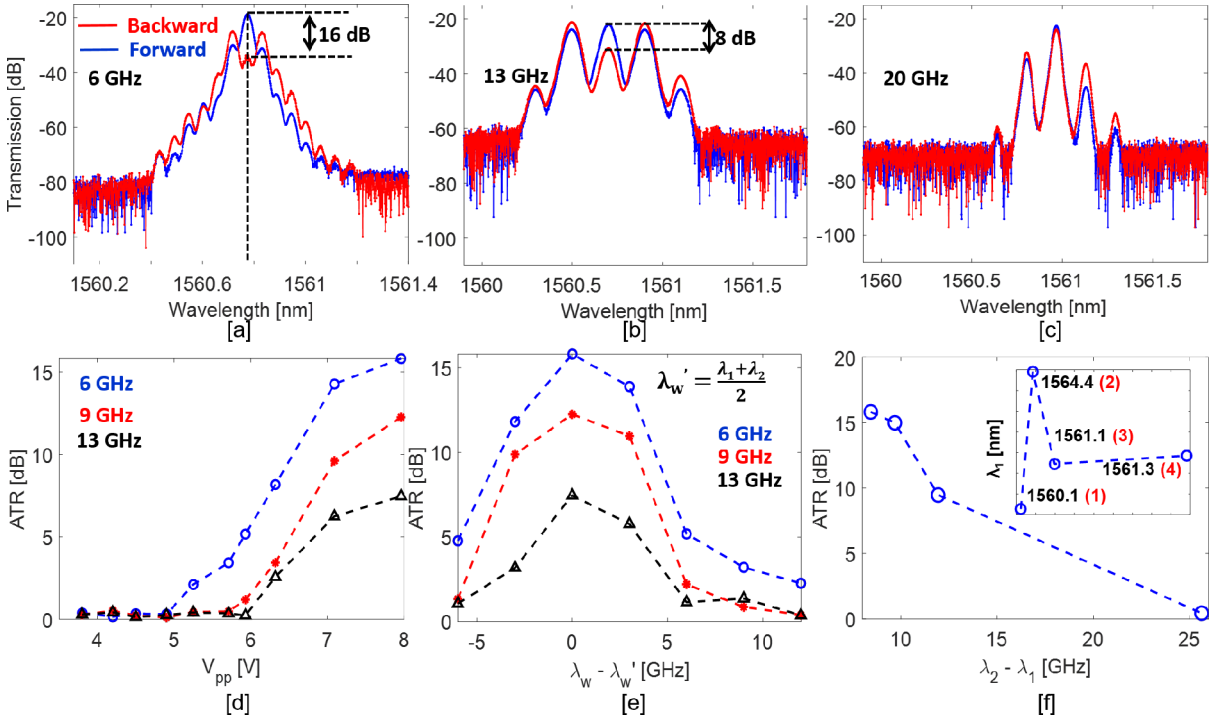

Figure 9. (a) Forward and backward transmission spectrum at 6 GHz driving frequency. (b, c) Same as part a for 13 and 20 GHz. (d) Variation of ATR as a function of V_{pp} obtained by changing the gain of the RF amplifier. (e) ATR variation when the working wavelength is changed from $\frac{\lambda_2 + \lambda_1}{2}$. (f) Change in ATR when $\lambda_2 - \lambda_1$ is changed by using different chips. The inset shows values of λ_1 for the four different chips used in this work.

Figure 9d shows the change in the ATR when the drive voltage V_{pp} is varied. A large V_{pp} implies a larger value of $\delta\omega/\Omega$ and hence a higher ATR. At 6 GHz, the ATR decreases from 16 dB at 8 V_{pp} to 0 dB when V_{pp} is less than 5 V (18 dBm). A similar trend is also seen at 9 and 13 GHz driving frequencies where the ATR decreases from 12 and 8 to 0 dB when V_{pp} is decreased. The lower value of the ATR at smaller values of V_{pp} arises from the low carrier suppression in the backward direction. Smaller V_{pp} results in a decreased $\delta\omega/\Omega$, and as we already discussed, a large $\delta\omega/\Omega$ is required for the complete conversion of power between the optical carrier and the sidebands.

We also analyzed the effect of the working wavelength λ_w on the ATR, and the result is shown in Figure 9e. The maximum ATR was obtained when $\lambda_w = \frac{\lambda_1 + \lambda_2}{2}$. At this particular working wavelength, the optical carrier is equally modulated by both modulators. A blue- or red-shift of the working wavelength λ_w will increase the carrier modulation in one MRM while simultaneously decreasing it in the other, which compromises the ATR. At Ω = 6 GHz, the ATR decreases from 16 to 5 dB when λ_w is blue-shifted by 6 GHz whereas it decreases to 4 dB for the a red-shift of the same amount. A similar trend is observed at the driving frequencies of 9 and 13 GHz where the ATR goes from a maximum of 12 and 8 dB, respectively, to a minimum of 0 dB.

We already stated that the difference between the resonance of both MRMs, despite having the same design parameters, is a

https://doi.org/10.1021/acsphotonics.1c00040
ACS Photonics XXXX, XXX, XXX−XXX

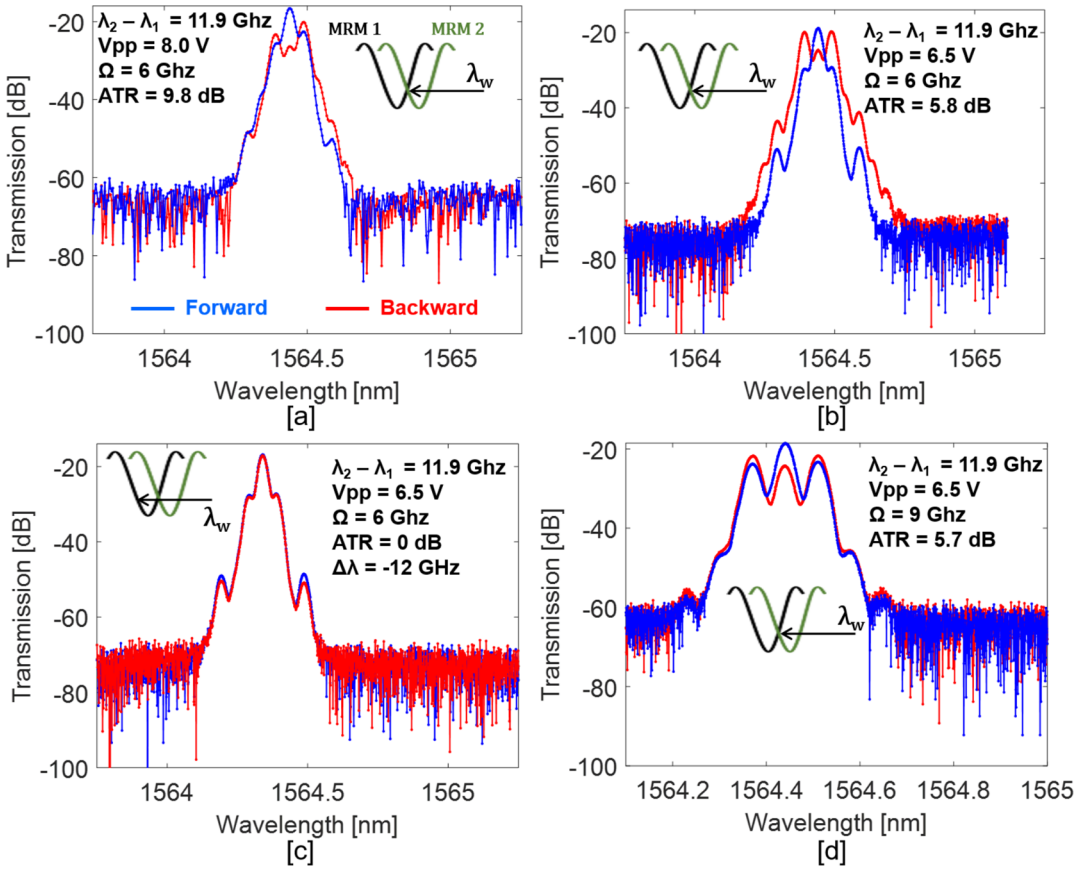

Figure 10. Variation of the sideband spectra with different modulation parameters: (a) $\lambda_2 - \lambda_1$ = 11.9 GHz at a V_{pp} of 8 V, (b) at V_{pp} of 6.5 V, (c) with the operating wavelength blue-shifted by 12 GHz, and (d) for 9 GHz at a V_{pp} of 6.5 V.

result of fabrication imperfections. Such imperfections lead to varying device parameters over the silicon wafer, and hence, it is crucial to study their effect on the optical nonreciprocal transmission. We selected four different chips from four random places on the wafer. In particular, we are interested in the variation in ATR as a function of the resonator misalignment $\lambda_2 - \lambda_1$. The inset in Figure 9f shows the measured variation of λ_1 on the four chips.

The wavelength λ_1 varies by 1.2 nm (150 GHz) between these 4 chips. The relative wavelength shift $\lambda_2 - \lambda_1$ is smaller and varies from 8.5 to 26 GHz over the different chips. The ATR (at Ω = 6 GHz) for the different values of $\lambda_2 - \lambda_1$ decreases from 16 dB when the $\lambda_2 - \lambda_1$ is 8.5 GHz to 0 dB when the separation is 26 GHz. A larger separation between λ_2 and λ_1 implies unequal modulation of the optical carrier from both MRMs, and if the separation becomes larger than the 3 dB line width of each MRM, there will be no nonreciprocal transmission. Integrating a heater with the ring resonator could easily overcome this misalignment.

Figure 10 shows the evolution of the optical carrier and sideband spectra with different modulation parameters. Figure 10a shows the carrier profile at 6 GHz driving frequency and a V_{pp} of 8.0 when $\lambda_2 - \lambda_1$ = 11.9 GHz and $\lambda_w = \frac{\lambda_1 + \lambda_2}{2}$. In the backward direction, the carrier is suppressed whereas it peaks in the forward direction. The insertion loss is 18 dB in the forward direction. When V_{pp} is reduced to 6.5 V (20.5 dBm), as shown in Figure 10b, the carrier suppression in the backward direction is less efficient, which results in a smaller ATR of 5.8 dB. When λ_w is blue-shifted by 12 GHz, as shown in Figure 10c, the difference between the forward and backward propagating carrier and the sidebands is very small. For this choice of λ_w, the optical carrier is modulated by only one of the MRMs while there is no interaction with the second MRM. Figure 10d shows the response at 9 GHz for the same parameters as in Figure 10b. As expected, a small ATR of 5.7 dB is observed due to the reduced value of $\delta\omega/\Omega$.

OUTLOOK

By optimizing the optical delay between the modulators, the insertion loss as well as ATR can be further improved. Our calculations show that a larger optical delay will allow for a complete conversion of the sideband power to the optical carrier that will reduce the insertion loss. For example, the optimum waveguide length in our work is around 5 mm. IMEC's iSIPP50G silicon photonics platform, which was used to fabricate our device, guarantees losses below 1.4 and 0.6 dB/cm for fully etched strip waveguides and 70 nm etched rib waveguides, respectively. Thus, the optimal optical delay line would introduce less than 1 dB extra loss while significantly enhancing the ATR. Moreover, using multimode waveguides, the waveguide propagation loss can be further reduced, down to 0.065−0.25 dB/cm.[41,42] The time delay between the cavities can also be improved by engineering the connecting waveguide's dispersion, e.g., by coupling the connecting waveguide with a passive cavity. The bandwidth of operation can be improved by incorporating efficient thermal tuners on the MRMs to tune the resonance locally. Since the nonreciprocal transmission relies on the conversion of optical energy between the carrier and the sidebands, an improved

https://doi.org/10.1021/acsphotonics.1c00040
ACS Photonics XXXX, XXX, XXX−XXX

scheme for efficient sideband generation can be used like increasing the ring quality factor or exploring other low-loss material platforms, among others, to further reduce the insertion loss.[34]

CONCLUSION

We proposed and demonstrated optical nonreciprocal transmission utilizing two cascaded microring modulators. Compared to designs based on traveling-wave phase modulators or MZIs, our scheme significantly reduces the device footprint. We carried out a rigorous analysis to study the cascaded modulator's behavior and demonstrate our findings using modulators fabricated in a commercial CMOS foundry. A very good agreement between simulations and the experiment is found. We reported an ATR (asymmetric transmission ratio) of 16 dB at a driving frequency of 6 GHz with an insertion loss of 18 dB. We also reported how the ATR changes with various device parameters and discussed the effect of fabrication variations on the performance. Our device enables the optical isolator's design with significantly reduced size and can be used in several photonic integrated circuit-based applications. Our simulations predict that, by optimizing the optical delay between both modulators, the ATR can be further improved, and the insertion loss can be decreased to a value close to zero.

AUTHOR INFORMATION

Corresponding Author

Awanish Pandey − *Department of Information Technology, Ghent University−imec, 9052 Gent, Belgium;* orcid.org/0000-0002-5489-1000; Email: awanish.pandey@ugent.be

Authors

Sarvagya Dwivedi − *imec, 3001 Leuven, Belgium*

Tang Zhenzhou − *Nanjing University of Aeronautics and Astronautics, Nanjing 210016, China*

Shilong Pan − *Nanjing University of Aeronautics and Astronautics, Nanjing 210016, China*

Dries Van Thourhout − *Department of Information Technology, Ghent University−imec, 9052 Gent, Belgium;* orcid.org/0000-0003-0111-431X

Complete contact information is available at: https://pubs.acs.org/10.1021/acsphotonics.1c00040

Notes

The authors declare no competing financial interest.

ACKNOWLEDGMENTS

A.P. is grateful to DST, Government of India, for his Postdoctoral Fellowship in Nano Science and Technology under Agreement 2019-2555. This work was supported by the EU commission through Grant Agreement 732894 (FET proactive HOT).

REFERENCES

(1) Thomson, D.; Zilkie, A.; Bowers, J. E.; Komljenovic, T.; Reed, G. T.; Vivien, L.; Marris-Morini, D.; Cassan, E.; Virot, L.; Fédéli, J. M.; Hartmann, J. M. Roadmap on silicon photonics. *J. Opt.* **2016**, *18*, 073003.

(2) Yang, K. Y.; Skarda, J.; Cotrufo, M.; Dutt, A.; Ahn, G. H.; Sawaby, M.; Vercruysse, D.; Arbabian, A.; Fan, S.; Alù, A.; Vučković, J. Inverse-designed non-reciprocal pulse router for chip-based LiDAR. *Nat. Photonics* **2020**, *14*, 369−374.

(3) Kittlaus, E. A.; Weigel, P. O.; Jones, W. M. Low-loss nonlinear optical isolators in silicon. *Nat. Photonics* **2020**, *14*, 338−339.

(4) Mock, A.; Sounas, D.; Alu, A. Magnet-free circulator based on spatiotemporal modulation of photonic crystal defect cavities. *ACS Photonics* **2019**, *6*, 2056−2066.

(5) Huang, D.; Pintus, P.; Bowers, J. E. Towards heterogeneous integration of optical isolators and circulators with lasers on silicon. *Opt. Mater. Express* **2018**, *8*, 2471−2483.

(6) Zhang, Y.; Du, Q.; Wang, C.; Fakhrul, T.; Liu, S.; Deng, L.; Huang, D.; Pintus, P.; Bowers, J.; Ross, C. A.; Hu, J. Monolithic integration of broadband optical isolators for polarization-diverse silicon photonics. *Optica* **2019**, *6*, 473−478.

(7) Zhang, Y.; Du, Q.; Wang, C.; Yan, W.; Deng, L.; Hu, J.; Ross, C. A.; Bi, L. Dysprosium substituted Ce: YIG thin films with perpendicular magnetic anisotropy for silicon integrated optical isolator applications. *APL Mater.* **2019**, *7*, 081119.

(8) Srinivasan, K.; Stadler, B. J. Magneto-optical materials and designs for integrated TE-and TM-mode planar waveguide isolators: a review. *Opt. Mater. Express* **2018**, *8*, 3307−3318.

(9) Du, Q.; Wang, C.; Zhang, Y.; Zhang, Y.; Fakhrul, T.; Zhang, W.; Goncalves, C.; Blanco, C.; Richardson, K.; Deng, L.; Ross, C. A. Monolithic on-chip magneto-optical isolator with 3 dB insertion loss and 40 dB isolation ratio. *ACS Photonics* **2018**, *5*, 5010−5016.

(10) Stadler, B. J.; Mizumoto, T. Integrated magneto-optical materials and isolators: a review. *IEEE Photonics J.* **2014**, *6*, 1−15.

(11) Huang, D.; Pintus, P.; Shoji, Y.; Morton, P.; Mizumoto, T.; Bowers, J. E. Integrated broadband Ce: YIG/Si Mach−Zehnder optical isolators with over 100 nm tuning range. *Opt. Lett.* **2017**, *42*, 4901−4904.

(12) Hutchings, D. C.; Holmes, B. M. A waveguide polarization toolset design based on mode beating. *IEEE Photonics J.* **2011**, *3*, 450−461.

(13) Poulton, C. G.; Pant, R.; Byrnes, A.; Fan, S.; Steel, M. J.; Eggleton, B. J. Design for broadband on-chip isolator using stimulated Brillouin scattering in dispersion-engineered chalcogenide waveguides. *Opt. Express* **2012**, *20*, 21235−21246.

(14) Zhou, X.; Chong, Y. D. PT symmetry breaking and nonlinear optical isolation in coupled microcavities. *Opt. Express* **2016**, *24*, 6916.

(15) Shi, Y.; Yu, Z.; Fan, S. Limitations of nonlinear optical isolators due to dynamic reciprocity. *Nat. Photonics* **2015**, *9*, 388−392.

(16) Nazari, F.; Bender, N.; Ramezani, H.; Moravvej-Farshi, M. K.; Christodoulides, D. N.; Kottos, T. Optical isolation via PT-smmetric nonlinear Fano resonances. *Opt. Express* **2014**, *22* (8), 9574−9584.

(17) Del Bino, L.; Silver, J. M.; Woodley, M. T.; Stebbings, S. L.; Zhao, X.; Del'Haye, P. Microresonator isolators and circulators based on the intrinsic nonreciprocity of the Kerr effect. *Optica* **2018**, *5* (3), 279−282.

(18) Sounas, D. L.; Alu, A. Non-reciprocal photonics based on time modulation. *Nat. Photonics* **2017**, *11*, 774−783.

(19) Yu, Z.; Fan, S. Complete optical isolation created by indirect interband photonic transitions. *Nat. Photonics* **2009**, *3*, 91−94.

(20) Shi, Y.; Lin, Q.; Minkov, M.; Fan, S. Nonreciprocal optical dissipation based on direction-dependent rabi splitting. *IEEE J. Sel. Top. Quantum Electron.* **2018**, *24*, 1−7.

(21) Sounas, D. L.; Alu, A. Angular-momentum-biased nanorings to realize magnetic-free integrated optical isolation. *ACS Photonics* **2014**, *1*, 198−204.

(22) Yu, Z.; Fan, S. Optical isolation based on nonreciprocal phase shift induced by interband photonic transitions. *Appl. Phys. Lett.* **2009**, *94*, 171116.

(23) Lin, Q.; Wang, J.; Fan, S. Compact dynamic optical isolator based on tandem phase modulators. *Opt. Lett.* **2019**, *44*, 2240−2243.

(24) Tzuang, L. D.; Fang, K.; Nussenzveig, P.; Fan, S.; Lipson, M. Non-reciprocal phase shift induced by an effective magnetic flux for light. *Nat. Photonics* **2014**, *8*, 701−705.

(25) Doerr, C. R.; Dupuis, N.; Zhang, L. Optical isolator using two tandem phase modulators. *Opt. Lett.* **2011**, *36*, 4293−4295.

(26) Bhandare, S.; Ibrahim, S. K.; Sandel, D.; Zhang, H.; Wust, F.; Noé, R. Novel nonmagnetic 30-dB traveling-wave single-sideband

optical isolator integrated in III/V material. *IEEE J. Sel. Top. Quantum Electron.* **2005**, *11*, 417−421.
(27) Doerr, C. R.; Chen, L.; Vermeulen, D. Silicon photonics broadband modulation-based isolator. *Opt. Express* **2014**, *22*, 4493−4498.
(28) Xu, Q.; Schmidt, B.; Shakya, J.; Lipson, M. Cascaded silicon micro-ring modulators for WDM optical interconnection. *Opt. Express* **2006**, *14*, 9431−9436.
(29) Pandey, A.; Jeyaselvan, V.; Selvaraja, S. K. Broadband optical single sideband generation using an ultra high shape-factor self coupled ring resonator. *Opt. Commun.* **2020**, *461*, 125224.
(30) Xu, Y.; Lin, J.; Dubé-Demers, R.; LaRochelle, S.; Rusch, L.; Shi, W. Integrated flexible-grid WDM transmitter using an optical frequency comb in microring modulators. *Opt. Lett.* **2018**, *43*, 1554−1557.
(31) Minkov, M.; Shi, Y.; Fan, S. Exact solution to the steady-state dynamics of a periodically modulated resonator. *APL Photonics* **2017**, *2*, 076101.
(32) Jain, A.; Arafin, S.; Dwivedi, S. CMOS compatible optical Isolator with tandem Ring Modulators. *IEEE Photonics Conference* **2019**, 1−2.
(33) Absil, P. P.; De Heyn, P.; Chen, H.; Verheyen, P.; Lepage, G.; Pantouvaki, M.; De Coster, J.; Khanna, A.; Drissi, Y.; Van Thourhout, D.; Van Campenhout, J. Imec iSiPP25G silicon photonics: a robust CMOS-based photonics technology platform. *Proc. SPIE* **2015**, *9367*, 93670V.
(34) Ehrlichman, Y.; Khilo, A.; Popović, M. A. Optimal design of a microring cavity optical modulator for efficient RF-to-optical conversion. *Opt. Express* **2018**, *26*, 2462−2477.
(35) Yu, H.; Ying, D.; Pantouvaki, M.; Van Campenhout, J.; Absil, P.; Hao, Y.; Yang, J.; Jiang, X. Trade-off between optical modulation amplitude and modulation bandwidth of silicon micro-ring modulators. *Opt. Express* **2014**, *22*, 15178−15189.
(36) Haus, H. A. *Waves and Fields in Optoelectronics*; Prentice-Hall, 1984.
(37) Shi, Y.; Shin, W.; Fan, S. Multi-frequency finite-difference frequency-domain algorithm for active nanophotonic device simulations. *Optica* **2016**, *3*, 1256−1259.
(38) Taflove, A.; Hagness, S. C. *Computational Electrodynamics: The Finite-Difference Time-Domain Method*, 3rd ed.; Artech House, 2005.
(39) Vercruysse, D.; Sapra, N. V.; Yang, K. Y.; Vučković, J. *Inverse-Designed Photonic Crystal Devices for Optical Beam Steering*. arXiv.org, 2021, arXiv:2102.00681. https://arxiv.org/abs/2102.00681.
(40) Miller, S. A.; Chang, Y. C.; Phare, C. T.; Shin, M. C.; Zadka, M.; Roberts, S. P.; Stern, B.; Ji, X.; Mohanty, A.; Gordillo, O. A. J.; Dave, U. D.; Lipson, M. Large-scale optical phased array using a low-power multi-pass silicon photonic platform. *Optica* **2020**, *7*, 3−6.
(41) Zhang, L.; Hong, S.; Wang, Y.; Yan, H.; Xie, Y.; Chen, T.; Zhang, M.; Yu, Z.; Shi, Y.; Liu, L.; Dai, D. *New-generation silicon photonics beyond the singlemode regime*. arXiv.org, 2021, arXiv:2104.04239. https://arxiv.org/abs/2104.04239.
(42) Idjadi, M. H.; Aflatouni, F. Nanophotonic phase noise filter in silicon. *Nat. Photonics* **2020**, *14*, 234−239.

https://doi.org/10.1021/acsphotonics.1c00040
ACS Photonics XXXX, XXX, XXX−XXX